A new method for short-duration transient detection in radio images: searching for transient sources in MeerKAT data of NGC 5068

S. Fijma [1][*] A. Rowlinson [1,2] R. A. M. J. Wijers [1] I. de Ruiter [1] W. J. G. de Blok,[2,3,4] S. Chastain,[5] A. J. van der Horst,[5] Z. S. Meyers,[1,6,7] K. van der Meulen,[1] R. Fender,[3,8] P. A. Woudt [3] A. Andersson [8] A. Zijlstra,[9] J. Healy[2] and F. M. Maccagni [2,10]

[1]*Anton Pannekoek Institute for Astronomy, University of Amsterdam, Science Park 904, NL-1098 XH Amsterdam, the Netherlands*
[2]*ASTRON, the Netherlands Institute for Radio Astronomy, Oude Hoogeveensedijk 4, NL-7991 PD Dwingeloo, the Netherlands*
[3]*Department of Astronomy, University of Cape Town, Private Bag X3, Rondebosch 7701, South Africa*
[4]*Kapteyn Astronomical Institute, University of Groningen, PO Box 800, NL-9700 AV Groningen, the Netherlands*
[5]*Department of Physics, The George Washington University, 725 21st Street NW, Washington, DC 20052, USA*
[6]*Deutsches Elektronen-Synchrotron DESY, Platanenallee 6, D-15738 Zeuthen, Germany*
[7]*Erlangen Center for Astroparticle Physics (ECAP), Friedrich-Alexander-Universität Erlangen-Nuremberg, D-91058 Erlangen, Germany*
[8]*Astrophysics, Department of Physics, University of Oxford, Denys Wilkinson Building, Keble Road, Oxford OX1 3RH, UK*
[9]*Jodrell Bank Centre for Astrophysics, Department of Physics and Astronomy, University of Manchester, Manchester M13 9PL, UK*
[10]*INAF - Osservatorio Astronomico di Cagliari, Via della Scienza 5, I-09047 Selargius (CA), Italy*

ABSTRACT

Transient surveys are a vital tool in exploring the dynamic Universe, with radio transients acting as beacons for explosive and highly energetic astrophysical phenomena. However, performing commensal transient surveys using radio imaging can require a significant amount of computing power, data storage, and time. With the instrumentation available to us, and with new and exciting radio interferometers in development, it is essential that we develop efficient methods to probe the radio transient sky. In this paper, we present results from a commensal short-duration transient survey, on time-scales of 8 s, 128 s, and 1 h, using data from the MeerKAT radio telescope. The data set used was obtained as part of a galaxy observing campaign, and we focus on the field of NGC 5068. We present a quick, wide-field imaging strategy to enable fast imaging of large data sets, and develop methods to efficiently filter detected transient candidates. No transient candidates were identified on the time-scales of 8 s, 128 s, and 1 h, leading to competitive limits on the transient surface densities of 6.7×10^{-5}, 1.1×10^{-3}, and 3.2×10^{-2} deg^{-1} at sensitivities of 56.4, 19.2, and 3.9 mJy following primary beam correction for the respective time-scales. We find one possible candidate that could be associated with a stellar flare, which was rejected due to strict image quality control. Further short time-scale radio observations of this candidate could give definite results about its origin.

Key words: radio continuum: general – radio continuum: transients.

1 INTRODUCTION

Exploring the radio transient sky has proven invaluable in studying highly energetic and/or explosive astrophysical phenomena. Searching for transient radio emission allows us to constrain the population of known source types, discover new types [such as fast radio bursts (FRBs); see Lorimer et al. 2007], investigate the associated sources for these events, and study the resulting kinetic feedback in the local environment (e.g. Fender et al. 2016).

With the continuing development of more sensitive radio telescopes with excellent uv- and sky-coverage, for example MeerKAT (Camilo 2018), the Australian SKA Precursor (ASKAP; Johnston et al. 2008), and the future Square Kilometer Array (SKA; Braun

et al. 2015), the search for transient sources in the radio sky has become of great interest to many researchers. So far, many types of transient source have been discovered, varying on time-scales from milliseconds to years. These can generally be divided in two categories: incoherent and coherent radio transients (see e.g. Pietka, Fender & Keane 2015, for an overview). Incoherent radio transients are proposed to emit through synchrotron radiation, and occur on time-scales above 1 s. Coherent radio transients are proposed to emit radiation in phase through Microwave Amplification by Stimulated Emission of Radiation or coherent synchrotron emission, and typically occur on short time-scales of the order of seconds or less. We can study these sources using radio observations in the image-domain, where the time-scale we can study is limited by the integration time (typically a few seconds), or using time series analysis, where a time resolution of microseconds or less is achievable. Furthermore, we can identify both transient and variable sources, where we define transient

[*] E-mail: s.c.fijma@uva.nl

sources in this work as sources that are newly detected during the observations.

Many teams have searched for radio transient sources in large surveys, using both imaging and time series analysis. In time series analysis, the main focus is on searching and describing radio pulsars, as well as on the detection of FRBs to determine their properties and likely progenitor systems (for a recent review see Petroff, Hessels & Lorimer 2022). In the image plane, a number of teams have searched large data sets for transient sources on time-scales from minutes to years (e.g. Driessen et al. 2020, 2022; Wang et al. 2021, 2023; Wang et al. 2022; Dobie et al. 2022, 2023; Andersson et al. 2023, see also Table A1). These studies are referred to as unbiased or commensal transient searches as they do not target known transient sources. At 1.4 GHz, commensal transient surveys have determined that radio transients are typically rare, but several have been identified (such as gamma-ray burst afterglows, stars, pulsars, galaxies, and active galactic nuclei, see e.g. Levinson et al. 2002; Thyagarajan et al. 2011; Aoki et al. 2014; Murphy et al. 2021; Andersson et al. 2022).

In this work, we focus on short-duration transient sources that are found via image-plane surveys. Interesting transient sources have been detected on sub-minute time-scales by a few surveys. For example, Hurley-Walker et al. (2022b) identified a periodic radio transient with pulses of duration 30–60 s in snapshot images produced from survey data obtained by the Murchison Widefield Array at around 150 MHz. Additionally, the detection of a 76 s period pulsar in time series analysis of MeerKAT observations and its subsequent detection in simultaneous 8 s snapshot images from MeerKAT (as part of observations by the MeerTRAP[1] and ThunderKAT[2] projects; Caleb et al. 2022) shows the high potential of using short-duration snapshot images to find new types of transient source such as slowly spinning neutron stars.

To search for rare transient sources, one would ideally survey the entire sky at all times so as to not miss any events. For example, the AARTFAAC All Sky Monitor achieves this for a large part of the low-frequency radio sky (10–90 MHz; Prasad et al. 2016; Kuiack et al. 2021) by generating radio images of 1 s in real time. Additionally, at high time resolution, the Canadian Hydrogen Intensity Mapping Experiment (CHIME; CHIME/FRB Collaboration 2018) and the Survey for Transient Astronomical Radio Emission (STARE2; Bochenek et al. 2020) survey a large part of the sky in real time for very short time-scale transients (≈ 1 ms) at frequencies of around 400–800 and 1280–1530 MHz, respectively. However, achieving this with image-plane surveys at 1.4 GHz is extremely challenging, due to the smaller fields of view of the facilities and the prohibitive computational costs of calibrating and imaging the data. Therefore, commensal transient surveys typically utilize archival data or data obtained by key survey projects obtained by the facilities (e.g. Bell et al. 2011; Hancock et al. 2016).

As radio transients are likely to be rare, large sky areas need to be processed to maximize the chance of detection. To cover as much sky area as possible, one would need observations covering a large field of view, or large numbers of fields with smaller sky area. Moreover, sensitive data are preferred, to be able to detect transient sources within a large range of peak luminosities. However, creating robust images on short time slices and performing a transient survey on these data still requires a significant amount of computing power, data storage, and time.

Imaging software like WSCLEAN (Offringa et al. 2014) enables efficient wide field imaging, and allows us to create time slices or snapshots in single observations. Using these time slices, transients can be studied on time-scales spanning the length of the observation (typically a few hours) to the integration time of the observation (typically a few seconds). However, despite the efficiencies in WSCLEAN, several of the steps are highly time-consuming. Cleaning the sources in the images is particularly slow as it is an iterative process. Additionally, software is used to detect and monitor sources, for example the LOFAR transients pipeline (TRAP; Swinbank et al. 2015). The time such processing pipelines take to analyse the images is highly dependent upon the number of sources per image. Thus, further optimization is required to significantly reduce the time it takes to conduct short-duration snapshot transient surveys.

In this paper, we present results from a MeerKAT short-duration transient survey, on time-scales of 8 s up to 1 h, conducted as part of the ThunderKAT large survey project to detect and monitor transient sources (Fender et al. 2016). We present a quick, wide-field imaging strategy to enable imaging of large data sets. As we focus on the search for short-duration radio transients, we aim not to monitor known sources in the field as this reduces the time required for subsequent analysis pipelines. In Section 2, we outline the data used in this paper and the calibration strategy. In Section 3, we outline the fast imaging strategy we used and its motivation. Section 4 outlines the image analysis steps including the detection and filtering of transient candidates. Section 5 compares our results to previous surveys conducted at 1.4 GHz.

2 DATA

The data used in this work were obtained as part of the large survey project MeerKAT HI Observations of Nearby Galactic Objects – Observing Southern Emitters (MHONGOOSE; de Blok et al. 2016), which aims to perform a deep survey of the neutral hydrogen distribution in a sample of galaxies using the MeerKAT radio telescope. We are able to perform a transient survey on their data as part of the ThunderKAT commensal search programme (Fender et al. 2016). We study an observation of NGC 5068, which was made as part of the early commissioning of MHONGOOSE on 2020 April 28. In this work we only use one observation to extensively test our developed method and to perform a detailed analysis on the obtained transient candidates.

NGC 5068 was observed with a total bandwidth of 3.27 MHz, a central frequency of 1.417 GHz, and 1001 frequency channels. The total length of the observation is 2.67×10^4 s or ≈ 7.41 h, and the visibilities were recorded every 8 s. J1939-6342 was used as the primary flux and bandpass calibrator, and J1311-2216 was used as the secondary phase calibrator. The target and secondary calibrator were observed sequentially, with 12 min spent on source followed by 2 min spent on the secondary calibrator. The resulting total time on target is $\approx 1.96 \times 10^4$ s or ≈ 5.45 h.

The data have been reduced by the MHONGOOSE team as described by Serra et al. (2019) and de Blok et al. (2020), using a pre-release version of the CARACal pipeline (Serra et al. 2019; Józsa et al. 2020). The pipeline uses components from various astronomy packages as one single execution. It first flags calibrator and target data using AOFlagger (Offringa et al. 2010). Then it performs a cross-calibration step using the primary and secondary calibrator, and a self-calibration step. We use this calibrated data set to perform our fast imaging strategy.

---

3 FAST IMAGING STRATEGY

As mentioned in Section 1, we aim to perform a computationally efficient transient survey. In this section, we outline the methods used to achieve this and an analysis of the quality of the images obtained.

3.1 Continuum subtraction

A continuum subtraction step is applied, where the self-calibrated continuum model is subtracted from the data in the uv-plane (de Blok et al. 2020). Any sources that are not present in the deep image are not detected throughout the full observation and are therefore not subtracted from the visibilities. Thus, the only sources remaining in the snapshot images are transient sources. Since this continuum subtraction can leave some artefacts, such as bright sources appearing as negative sources in the full image, we cannot yet use this to identify variable sources.

The continuum extraction step speeds up analysis twofold. First, the removal of sources from the visibilities leads to faster processing by WSCLEAN. Secondly, by only keeping sources that are transient candidates the subsequent image analysis steps using TRAP are significantly faster.

An additional positive consequence of this step is that the final snapshot image rms noise is significantly lower than for the non-subtracted images and is approaching thermal noise. This is because the confusion noise component of the rms in the snapshot image is being drastically reduced. Therefore, we are also maximizing the sensitivity of the transient survey we are conducting.

Applying a continuum subtraction to (snapshot) images has only been applied very recently in radio transient surveys. Hurley-Walker et al. (2022b) detected an 18 min periodic radio transient at low frequencies during a drift-scan of the GLEAM-X survey (Hurley-Walker et al. 2022a). To optimize the imaging speed, they imaged 0.5 s snapshots where they subtract the continuum model but add the transient source back in. Moreover, Caleb et al. (2022) initially discovered a 76 s slow-spin pulsar as a serendipitous single-pulse discovery in the Vela X-1 field using MeerTRAP (Stappers 2016). To expedite the production of per-integration time images, they subtracted the continuum model from the data, and then re-imaged the data on 2 to 8 s time-scales. Finally, Dobie et al. (2023) apply a fast-imaging method by subtracting the continuum model from the data, and then imaged them at 15 min time-scale to perform a blind transient and variable survey. However, this can be further optimized with the next step.

3.2 Snapshot imaging

As briefly motivated in Section 1, we image the data using WSCLEAN (Offringa et al. 2014). To study transient sources at the time-scales of 1 h, 128 s, and 8 s, we create 6, 153, and 2454 time slices of the data, respectively. We create these time slices using the `IntervalsOut` command. The images per time slice are created at three frequency bands (1.416, 1.417, 1.418 GHz), together with a combined multifrequency summed (MFS) image. This allows us to create improved frequency-integrated images, as well as to perform checks on the individual frequency images for transient candidates.

Using the `FitBeam` command when imaging the full data set, we fit the shape of the point spread function and use this to determine the size and position angle of the restoring beam, which corresponds to 7.79 arcsec × 6.68 arcsec for the restoring beam size in the continuum-subtracted data. Based on the restoring beam size, we set
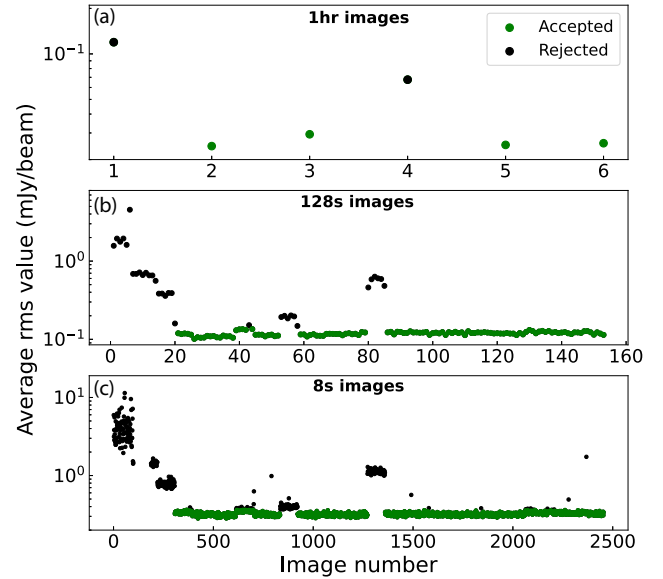
Figure 1. The average rms values for all images for each time-scale. The top panel (a) shows the average rms values for the 1 h time-scale images, the middle panel (b) for the 128 s time-scale images, and the bottom panel (c) for the 8 s time-scale images. The green data points indicate the accepted images for the transient survey, and the black data points indicate the rejected images.

the `PixelScale` setting to 2 arcsec, so that the beam would cover around 9 to 10 pixels in the image. The image size was based on the amount of data that could be efficiently imaged, i.e. where the run time was not excessive, which is 5120×5120 pixels or $2.87° \times 2.87°$ in size. The weighting scheme is set to Briggs weighting, with the robustness parameter set to 0.

As mentioned in Section 1, the standard imaging step of cleaning is very slow due to it being an iterative process. As we are imaging continuum-subtracted data, the only sources should be transients and we expect the majority of images to contain no sources. Therefore, we decide to skip the time-consuming cleaning process and use the 'dirty' images in our further analysis. This has been applied by Wang et al. (2021) on continuum-subtracted snapshots to study radio variables, and by Wang et al. (2023) to perform a blind transient survey on ASKAP data. Additionally, we do not perform a primary beam correction for the imaging as this also slows down processing.

3.3 Image quality control

Once we have created time sliced images for the 1 h, 128 s, and 8 s time-scales for our data, we evaluate the quality of the images by measuring the average rms noise variation in the inner one-eighth of the images. This is measured for each image when using the TRAP, which will be discussed in detail in the next section. It should be noted that there is some faint emission in the centre of the image as a result of an incomplete subtraction of the continuum emission of galaxy NGC 5068. However, as this only covers the inner 125th of the image and only faint emission remains, we can use the average rms noise calculated in the inner one-eighth of the images.

In Fig. 1 we show the average rms noise for the MFS images per time-scale. Based on this distribution, we iteratively reject images where the rms noise deviates more than 3σ from the mean. These images likely have high values for the average rms noise due to poor uv-coverage, a turbulent ionosphere, radio-frequency interference

(RFI), and/or poor calibration of the data, as discussed by e.g. Rowlinson et al. (2016). 33 out of 153 images (or 21.6 per cent) in the 128 s time-scale are rejected, and 528 out of 2454 images (or 21.5 per cent) in the 8 s time-scale are rejected. Furthermore, we manually reject two out of six images (or 33.3 per cent) in the 1 h time-scale, as they are evidently poor-quality images but are not removed using the 3σ clip due to the low number of images. The remaining images are used for our transient survey.

4 ANALYSIS

4.1 Detecting transient candidates

To detect transient sources in the images, we use the TRAP (Release 4.0; Swinbank et al. 2015). TRAP has several settings we can tweak to optimize our transient searches, but most of the default TRAP settings are appropriate for our survey. We set `force_beam` to `True`, so TRAP sets all source fits assuming that all sources have the size, shape, and orientation of the restoring beam and keeps these parameters constant. The `new_source_sigma_margin` parameter determines the margin of error (as a multiple of the rms of the previous best image) for which a new candidate is considered a false positive resulting from fluctuations around the detection threshold. We set this to 0, so we can consider all transient candidates resulting from our survey. The `extraction_radius` is the radius in pixels in which TRAP will search for candidates. We evaluate the noise distribution throughout the image, and the edges were not considerably noisier than the centre. This is expected, since we did not apply a primary beam correction in the images. We did apply a primary beam correction to the transient surface densities and sensitivities reported in Section 5.

The radius is usually set to around the primary beam size in commensal transient surveys, as the telescope is most sensitive here. For the MeerKAT telescope, the half width at half-maximum (HWHM) of the telescope beam at 1.42 GHz is $\approx 0.52°$ (Mauch et al. 2020). Because of the noise distribution in our images, and to test out our method for a larger area of the images, we decided to include a large extraction radius in our survey, and to set this at 2500 pixels (or around $1.4°$). This can be reconsidered for future surveys to improve efficiency.

Lastly, we determine the `detection_threshold` setting, which is expressed as a multiple of the rms noise. To limit the amount of false positive detections, we calculate the `detection_threshold` such that we would expect <1 false positive detections caused by noise. In Section 2 we mentioned that we chose the pixel scale such that the restoring beam size would be ≈ 10 pixels. A false positive detection could then be the result of noise when around 10 pixels have values in Jy beam^{-1} exceeding the detection threshold. We can expect this assuming that the noise in a radio image follows a Gaussian distribution and that the noise is random, caused by e.g. contributions of sky and receiver thermal noise, so the noise pixel values are independent of each other.

A Gaussian pixel distribution may not always be applicable for radio images. Noise can be correlated in between different images and within individual images (e.g. Rowlinson et al. 2016), which changes the distribution. Moreover, calibration artefacts and side lobes present in the image also affect the distribution. Therefore, we fit a Gaussian distribution to a random sample of the 1 h, 128 s, and 8 s images, to see if this assumption would hold for our data. We find that a Gaussian distribution fits our data well. We show an example in Fig. 2.
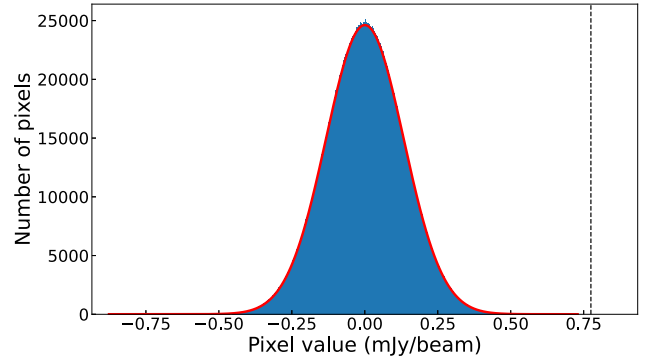
Figure 2. The pixel value distribution of an example image (image 39) for the 128 s time-scale shown in blue, with a fitted Gaussian distribution shown in red. The corresponding detection threshold for this data set, at 5.8σ, is indicated with a black dashed line.

Table 1. The number of images used for the transient survey for each time-scale. The total number of images are filtered using quality control (QC) steps described in Section 3.3. The detection threshold is calculated in Section 4.1, based on expecting < 1 false positive per time-scale. We show the initial number of transient candidates detected in the filtered images.

Time-scale	Total number of images	Number of images after QC	Detection threshold	Number of candidates
1 h	6	4	5.3σ	17
128 s	153	120	5.8σ	8
8 s	2454	1926	6.3σ	4

We calculate the detection threshold based on the probability that we encounter 10 pixels exceeding the detection threshold for the total number of pixels per data set for the 1 h, 128 s, and 8 s time-scales. This can be expressed as $Pr(X \leq x) = 1 - \frac{1}{N}$. N is the total number of beams per data set, or the total number of pixels in the data set divided by the number of pixels in the restoring beam. We calculate the value of x expressed in σ (i.e. the threshold) for this probability using the per cent point function (or inverse cumulative distribution function) for the Gaussian distributions of the images per time-scale using the `scipy stats norm ppf` functionality (Virtanen et al. 2020). It is not likely for 10 randomly distributed noise pixels exceeding the detection threshold to all appear in the same location in the image, and in the shape and size of the restoring beam. Therefore, this method is mainly used to get a good approximation for the detection threshold. In Table 1 we show the calculated detection thresholds per time-scale data set, and the total number of candidates we obtain for each of the data sets. The thresholds were calculated for a random sample of accepted images per time-scale, which gave consistent values for the threshold to three significant digits for each time-scale. The thresholds were then scaled to all pixels for each time-scale data set.

4.2 Filtering transient candidates

Besides false positive detections caused by noise, more types of false positive are expected in radio transient surveys. Gourdji et al. (2022) describe some categories of detected transient candidates, including:

(i) imaging artefacts from sidelobes around bright sources;

(ii) extended sources with fit parameters that differ significantly between images preventing them from being associated with one another by TRAP;

(iii) faint sources detected around the detection threshold in an image, but that were undetected in at least the first image due to higher local rms.

To separate false positive detections from true astrophysical detections, we employ a number of filtering steps to our lists of transient candidates per time-scale data set.

As described in Section 4.1, we initially filter false positive detections caused by noise using the calculated `detection_threshold` per time-scale data set. In Table 1 we show the total amount of candidates detected using the detection thresholds.

The source finder used in TRAP (PYSE; Carbone et al. 2018) calculates the noise in an image by dividing the source extraction region into a grid. Rowlinson et al. (2016) find that the local rms is not accurately calculated close to the extraction radius by TRAP, because TRAP does not model the rms noise beyond the source extraction region. Therefore, we reject any candidates with a distance greater than 2460 pixels from the centre of the image. Because trap uses bilinear interpolation in calculating the background and rms maps (Swinbank et al. 2015), this results in inaccurate calculations and thus can result in false positive detections close to the extraction radius. The background size used to calculate the local rms is set to 50×50 pixels. We expect the rms to be accurately calculated for sources in the middle of this box when the entire box is included in the extraction radius. Therefore, we filter any sources closer than half the diagonal of the background box to the extraction radius, which we round up to 40 pixels. As the extraction radius for all transient searches is set to 2500 pixels, we choose to reject any candidates with a distance greater than 2460 pixels from the centre of the image. This step resulted in four out of four candidates in the 8 s time-scale data to be rejected. No candidates in other time-scales were rejected using this step.

We also perform a visual inspection of the transient candidates. The aforementioned types of false positive detection are easily distinguished by eye from potential astrophysical transient sources (see e.g. fig. A1 in Gourdji et al. 2022). Furthermore, we also identify an additional false positive detection type caused by detected remnants from the applied continuum subtraction. These appear like bright points in noisy areas in the location of bright sources in the original data. For our visual inspection, we only accept transient candidates in the shape of the restoring beam and do not fit the description of the false positive detection types. Moreover, we filter any candidates that are present in the image of the full observation, as the remaining sources would be artefacts of the continuum subtraction, and as we are only interested in detecting transient sources. Eight out of eight candidates in the 128 s time-scale data are rejected using this step, and 12 out of 17 candidates the 1 h time-scale data.

Once we obtain promising candidates from the visual inspection, we proceed to use the TRAP monitoring functionality to monitor the location of the transient candidates in all images of the 1 h, 128 s, and 8 s time-scales, to obtain light curves of the candidates on these time-scales. This allows us to check if variations in the light curves are significant, or a result of the signal-to-noise ratio fluctuating around the detection threshold. We show an example of a rejected candidate in Fig. 3. It also allows us to characterize the behaviour of the candidate sources and the area in which they are located. This results in three out of five candidates in the 1 h time-scale data to be rejected.

If the variations are significant compared to the noise measurements before and after the transient behaviour, we proceed to monitor noise surrounding the candidates. Some detections can result from a local increase in the noise, ionospheric effects, poor calibration,
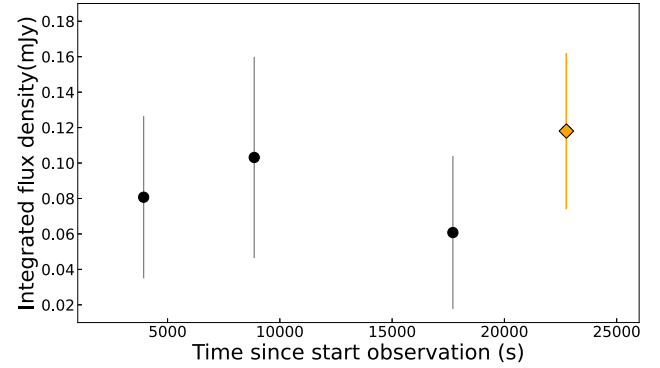

Figure 3. The light curve of a rejected candidate detected in the 1 h time-scale data, where the TRAP detection is shown with the yellow diamond.
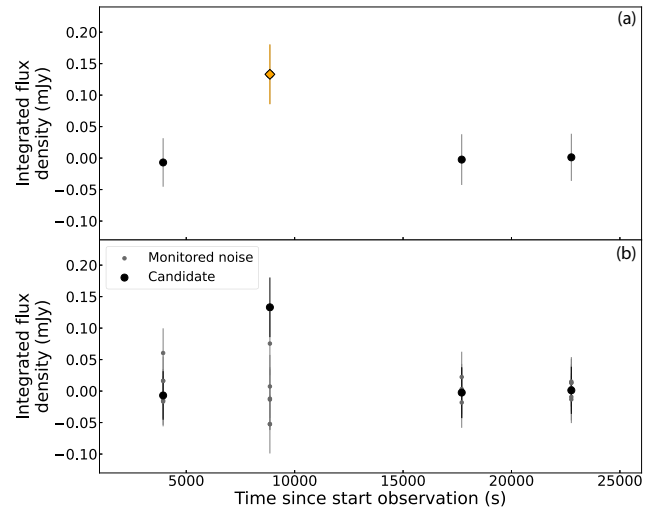
Figure 4. The light curve of a rejected candidate detected in the 1 h time-scale. Panel (a) shows the light curve from the candidate where the TRAP detection is shown with the yellow diamond. Panel (b) shows the light curve of the candidate using black data points, as well as light curves of five noise points which were randomly selected in the vicinity using grey data points (see Section 4.2).

or high RFI. Therefore, we create and check the light curves of five random points surrounding the candidates. We monitor these points in the image where the candidate was initially detected, as well as 10 images before and 10 images after this image, to analyse the noise close in time to the detection. Furthermore, we generate the random points at least a distance of five times the size of the restoring beam from the candidates, to limit the effects of imaging artefacts and residual dirty beam effects close to the source, see e.g. de Ruiter et al. (2021). We also select the points within a distance of 2 arcmin (approximately 15 times the major axis of the restoring beam), so that the points are representative for monitoring noise specifically close to the candidate. If the statistical errors for the integrated flux density for one or more of the random (noise) points overlap with the statistical errors for the integrated flux density of the candidate during the observed variation in the light curve, i.e. if the peak of the detection does not deviate significantly from the noise, we reject the candidate. We show an example in Fig. 4. We also reject any candidates where the noise shows a similar evolution in flux as the flux of the candidate. This results in two out of two candidates in the 1 h time-scale data to be rejected.
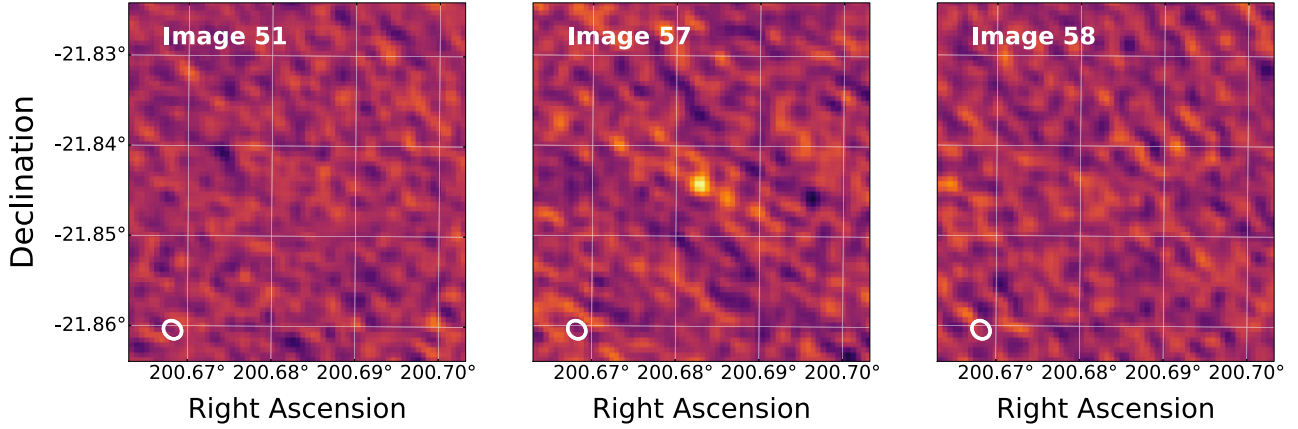
Figure 5. MeerKAT images for the 128 s time-scale showing the location of the rejected transient candidate, each with a dimension of 2.4 arcmin × 2.4 arcmin. The middle panel shows the image in which the candidate was detected, image 57, with a signal-to-noise ratio of 6.02σ. The left panel shows image 51, which is the first accepted image (based on quality control, see Section 3.3) preceding image 57. The right panel shows image image 58, which is the first accepted image following image 57. The contour of the shape and size of the restoring beam as determined for full data set by TRAP is shown in white in the lower left corner.

In summary, no transient candidates pass all of the filtering criteria for this survey.

4.3 Rejected transient candidate

One candidate passed the filtering strategies in a pilot survey of the data, when the quality checks for the images were less conservative. However, after performing the image rms analysis for our final survey, the image in which we detected the candidate (image 57, see Fig. 1) was rejected. Although this candidate is not considered as a potential astrophysical transient source for our survey, we do believe it would be interesting to consider if the data are reprocessed or in future observations of the field. Moreover, we were also able to test our methodology of how a transient candidate from this type of data set would be processed.

The candidate was detected in the 128 s time-scale data set at right ascension (RA) 200.683° and declination (Dec.) −21.844° with a signal-to-noise ratio of 6.02σ and an integrated flux density of 0.90 ± 0.23 mJy without primary beam correction. In Fig. 5 we show the transient candidate before, during, and after its detection in the 128 s time-scale data set. In Fig. 6 we show the light curves of the transient candidate, using the 128 s data where the candidate was initially detected, and using the 8 s images to improve the time resolution of the light curve. We find a clear peak in the 8 s light curve at the time of the detection, which lasts around ≈64 s. Thus, the source is detected in multiple snapshots and in images with different time slicing. This adds strength to the candidate as it is then unlikely to be caused by features in the radio images such as side lobes or incomplete source subtractions. This is because imaging artefacts tend to appear in different locations within the images when using different uv-coverage (i.e. changes in integration time or observing frequency).

The signal-to-noise ratio of the transient candidate exceeds the detection threshold for the 128 s data of 5.8σ. When studying the image, the candidate appears point-like and has the shape of the restoring beam (as determined by TRAP for the full data set), with no excessive noise or artefacts surrounding the candidate. The light curve shows a clear variation from the flux in other images, and the candidate is within 2460 pixels of the centre of the image.
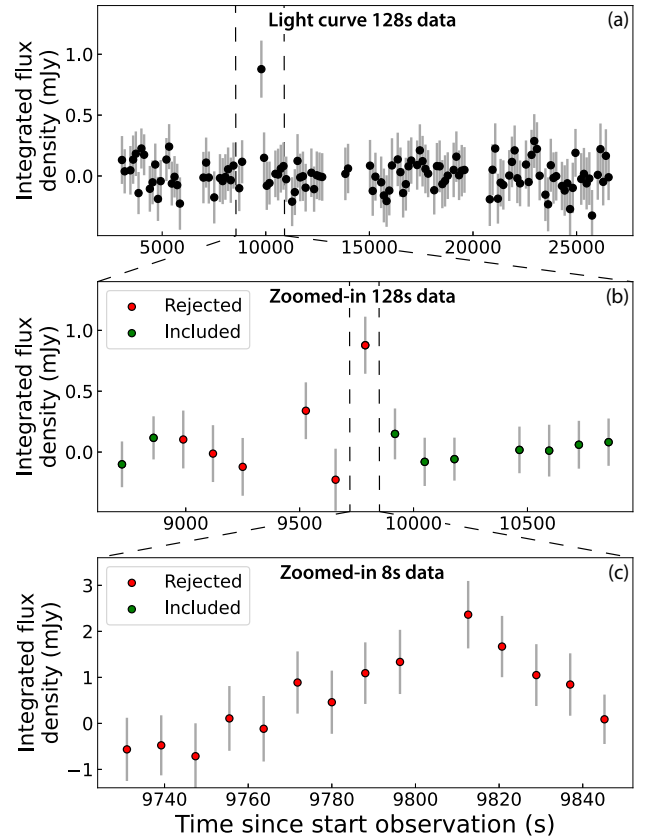
Figure 6. The integrated flux density in mJy measured by TRAP in each image at the location of the rejected transient candidate, plotted against the time since the start of the observation. Panel (a): The light curve for all images for the full 128 s time-scale data set, showing a peak in 1 image where the candidate was detected. Panel (b): The light curve of 15 images around the detection of the candidate of the 128 s time-scale data set. The images rejected by our quality control are shown in red, and the accepted images are shown in green. Panel (c): The light curve of the 8 s time-scale images around the time of the detection in the 128 s time-scale image.
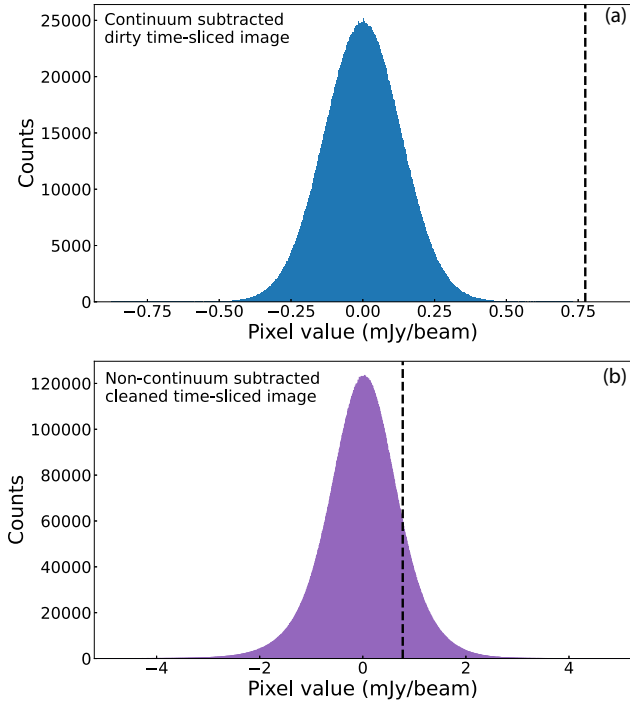
Figure 7. The pixel value distributions for an example image (image 39) from the 128 s data set. Panel (a) shows the distribution for the dirty continuum-subtracted data, and panel (b) for the cleaned non-continuum-subtracted data. The black dotted line shows the pixel value for the 5.8σ detection threshold as determined for the dirty continuum-subtracted image.

Furthermore, we monitored random points surrounding the candidate to study the noise, and we find that the light curves of the random noise points do not follow the same trend as the light curve of the candidate.

Lastly, we also check the images of the different frequency bands. RFI could also result in a false positive detection in radio images, but RFI generally spans a more limited frequency range than the frequency range of our observation (see e.g. Offringa et al. 2010). Therefore, if this is a false positive detection resulting from RFI, we expect to only identify emission in one or two of the frequency band images. We identify point-like emission at the location of the candidate in all three frequency band images. Moreover, RFI would be visible across the image, as a satellite or plane would leave multiple candidates in a line across the image (e.g. Kuiack et al. 2021). In this case, we would also expect more features in the noise, which we do not identify for this candidate. Therefore, we deem the scenario of RFI causing a false positive detection for this candidate to be unlikely.

Our method for the transient survey involves analysing the dirty continuum-subtracted data. To study the candidate further, we created cleaned images of the original non-continuum-subtracted data, to see if we detect the transient candidate data in these images as well. We were not able to recover this transient candidate in the cleaned non-continuum-subtracted data. However, we find that the (re)imaged cleaned time slice images from the non-continuum-subtracted data have higher rms noise than the original time sliced dirty images using continuum-subtracted data. This is based on analysing the pixel value distribution (we show an example in Fig. 7), as well as studying the integrated flux density of random points in the images. As noted in Section 3.2, without the continuum subtraction we are not able to probe as deep as in our original survey due to confusion noise.

We perform a catalogue search to see if we can find an associated source for the candidate. One source is detected by PanSTARRS (Chambers et al. 2016), *Gaia* DR3 (Gaia Collaboration 2016), and 2MASS (Skrutskie et al. 2006), at RA 200.68070925(6)° and Dec. −21.84227554(4)° for *Gaia* DR3 (with a proper motion of 5.50 and −11.1 mas yr^{-1} for the RA and Dec., respectively). This is within 10 arcsec of the position of the transient candidate, which is the default systematic positional uncertainty measured with TRAP. The PanSTARRS observed magnitudes are $g = 19.735(11)$, $r = 18.801(6)$, and $i = 18.362(4)$. These give colours of $r - i = 0.439(7)$ and $g - r = 0.934(12)$, which are consistent with a K-type star on the main sequence (see fig. 1 in Finlator et al. 2000). Therefore, the duration of the transient and its optical association are consistent with this transient being a stellar flare.

Calculations in Yu, Zijlstra & Jiang (2021) of expected flare star densities predict one flare from an M-dwarf brighter than 1 mJy (at 5 GHz) over 400 square degrees in an 8 h integration, giving a predicted density of 2.5×10^{-3} per square degree for an 8 h observation. This gives a probability of around 2 per cent to detect an M-dwarf flare, with the fraction of flares decreasing for earlier types, i.e. for the proposed K-type star. Moreover, based on photometric data of the associated optical source from the Catalina Real-Time Transient Survey Data Release 2 (Drake et al. 2009), no flaring behaviour is found. Follow-up research using short time-scale radio and optical observations are thus needed to further study this transient and its potential optical counterpart.

Because of the filtering method we employ for the rejection of low-quality images, we cannot justify including this candidate as a potential astrophysical transient source for our survey. The average rms for the image where this candidate was initially detected, image 57, is 0.15 mJy beam^{-1}, so 4.5σ removed from the mean of 0.12 mJy beam^{-1}. The previous five images (52 to 56) were also rejected using this method; however, the average rms values for these images deviated around 10σ to 13σ from the mean. The decision to include or exclude image 57 is therefore somewhat of an edge case. Generally, we find that applying an image filtering method is necessary for our survey, as including low-quality images results in detecting a large number of false positive candidates. None the less, from this result it appears that our image filtering method could be too conservative for our transient survey, meaning that we might miss real astrophysical transient sources in the data.

We tried different methods for filtering images based on the rms. We attempted to calculate the value for the mean and standard deviation of the entire image data set, and only reject images deviating more than 3σ from the mean once, instead of using iterative clipping. We also tried iteratively clipping images deviating 4σ from the mean instead of 3σ. However, we found that our current method was more appropriate, because otherwise we would include evidently low-quality images as well.

This transient candidate, although rejected in the final analysis, suggests that there may indeed be exciting transients to be found on these time-scales and – given that this was only a small data set – they may even be plentiful. If this transient is indeed a stellar flare, then we expect to find more flares from this source in the full MHONGOOSE observations of this field.

5 TRANSIENT SURFACE DENSITY

In this section, we compare our transient survey to previous transient surveys at $\approx$1.4 GHz (given in Table A1 and obtained from Mooley

et al. 2016).[3] These surveys are typically compared using the transient surface density, which is the number of transients detected per square degree surveyed, and the sensitivity of the survey, which is defined as the faintest detectable transient in the survey.

For each image, we extracted sources out to a radius of 1.4 deg giving a sky area of ≈5.9 square degrees per image. Following the method developed in Rowlinson et al. (2016), we can calculate the typical sensitivity as a function of radius by dividing the sensitivity in the centre of the image by the primary beam response. The MeerKAT primary beam main lobe is well modelled using a cosine aperture taper (Condon & Ransom 2016) and this model is provided using KATBEAM.[4] For each observing frequency, we use KATBEAM to model the 2D primary beam response and take a cross-section through the beam response from a radius of 0 to the search radius in degrees giving beam(r). We then obtain the sensitivity as a function of radius using

$$\text{Sensitivity}(r) = \frac{\text{Detection threshold} \cdot \text{RMS}_c}{\text{beam}(r)}, \quad (1)$$

where the detection threshold in σ is given in Table 1 and the RMS$_c$ is the average rms noise in the centre of the images for a given search time-scale. We calculate this sensitivity curve for each image and then combine the results by summing the total area searched across all images for given sensitivity bins.

The noise is increased as a result of the primary beam correction, reducing the sensitivity at the edge of the beam. This is important to note when comparing this result to the average rms values shown in Fig. 1, which is calculated in the inner one-eighth of each image without primary beam correction.

To calculate the total transient surface density probed, as a function of sensitivity, we first calculate the area enclosed within each radius and multiply it by the number of images surveyed at each time-scale. For a 95 per cent confidence limit, following e.g. Bell et al. (2014) and Rowlinson et al. (2016), the transient surface density is given by

$$\rho(r) = \frac{3}{A(r) \cdot N_{\text{imgs}}}, \quad (2)$$

where $A(r)$ is the area probed in one image out to a radius of r and N_{imgs} is the number of images probed for each time-scale surveyed. Combining this equation with the areas calculated using equation (1) for given sensitivity bins, we can calculate the transient surface density as a function of the transient search sensitivity.

Using equations (1) and (2), we plot the transient surface density limits as a function of the sensitivity in Fig. 8 for each of the three time-scales probed in this survey (red curves). The red diamonds show the lowest surface density probed (i.e. the largest sky area surveyed) at the worst sensitivity and these values are given in Table A1.

On 8 s time-scales, we find an upper limit on the transient surface density of 6.7×10^{-5} deg^{-1} at a sensitivity of 56.4 mJy. This is one of the first commensal transient surveys of its kind on 8 s time-scales at 1.4 GHz, together with other MeerKAT studies (Chastain et al. 2023). On these time-scales, we might expect to find sources such as slow pulsars. Recently a slow pulsar, J0901-4046, was detected using high time domain and imaging data obtained as part of the MeerTRAP and ThunderKAT projects (Caleb et al. 2022). J0901-4046 has a 76 s spin period and pulses from this unusual pulsar were clearly detected in 8 s snapshot images created using the MeerKAT

imaging data and localized to arcsecond precision. Additionally, a periodic radio transient has been discovered in snapshot imaging at around 150 MHz by the Murchison Widefield Array; with a spin period of 18.18 min and pulses of 30–60 s duration (Hurley-Walker et al. 2022b). Hurley-Walker et al. (2022b) suggest that this source may be a radio magnetar due to its unusual properties. The pulsar and candidate magnetar detections demonstrate that these sources would be detectable in commensal transient searches using MeerKAT observations, such as the data set presented in this paper. However, this field is at high Galactic latitude ($b = 41$ deg) and, hence, we expect the number density of pulsars to be very low in this field.
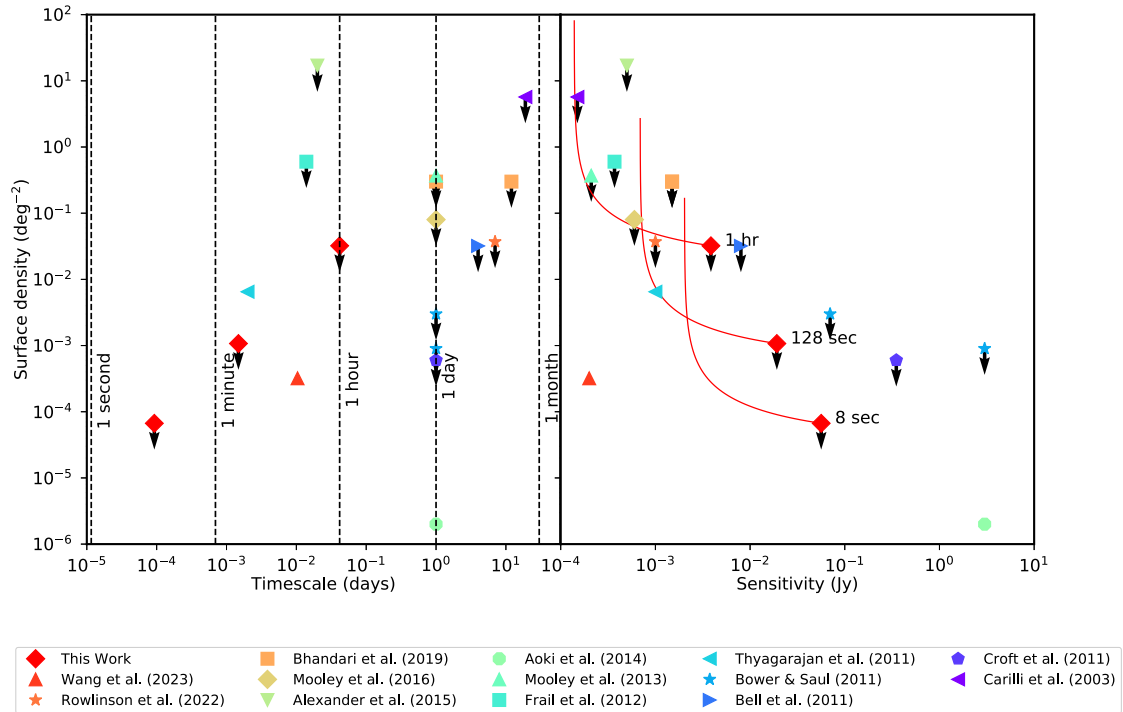
On 128 s time-scales, we find an upper limit on the transient surface density of 1.1×10^{-3} deg^{-1} at a sensitivity of 19.2 mJy. As shown in Fig. 8 and outlined above, this limit is best represented by a curved line taking into account the improved sensitivity in the inner regions of the images. This curved line passes through a data point obtained by Thyagarajan et al. (2011), who conducted a commensal transient survey on a similar time-scale of 3 min. The observations processed by Thyagarajan et al. (2011) comprised of 65 000 images from the FIRST survey (Becker, White & Helfand 1995) at 1.4 GHz. They detected 57 sources identified as being transient, with most having no archival association. As the line representing our survey passes through the data point of Thyagarajan et al. (2011), we can deduce that we would expect to detect approximately one transient source in our observations. Although it has several caveats, the source presented in Section 4.3 would be consistent with our expectations from Thyagarajan et al. (2011). We also note that with just 7.41 h of MeerKAT data, we are able to match the constraints obtained using the entire FIRST survey. Moreover, Wang et al. (2023) find three single flare transients in 754 images when conducting a commensal transient survey on a time-scale of 15 min at 1.4 GHz. This provides a more constraining transient surface density compared to the upper limits we find for the 128 s and 1 h time-scales. The sensitivity of this survey is comparable to the sensitivity probed at the 1 h time-scales at the centre of the image, but is around one order of magnitude more sensitive when compared to the edge of the search radius, and one to two orders of magnitude more sensitive when compared to the 128 s time-scale. Since the probed time-scale of this survey is different than those probed in this work, we cannot directly compare this. However, important to note is that the three discovered transients have been identified as radio stars, and appear to be transient on either minute or 1 h time-scales when studying the dynamic spectra and the 15 min light curves. Applying the presented method to the full MHONGOOSE data set will allow us to accurately compare the transient surface density constraints with those presented in Wang et al. (2023).

Two other transient sources have been detected on the several minutes time-scales at lower radio frequencies. The first source is GCRT 1745, known as the 'Galactic Burper', and emits flares of duration ≈10 min with a periodicity of 77 min (Hyman et al. 2005). The nature of the 'Galactic Burper' remains unknown, with a leading theory being a magnetar. As the Galactic Burper is located near the Galactic Centre, it is unlikely that the observations presented in this paper would detect a similar object due to their high Galactic latitude. The second source at low radio frequencies was found well off the Galactic Plane in imaging observations obtained by LOFAR (Stewart et al. 2016). This source had a duration of a few minutes, a poorly constrained flux density of 15–25 Jy and was detected at 60 MHz. The nature of this source also remains unknown. Due to the significant difference in observing frequency and unknown source spectrum, it is unclear if transients of this type would be detectable in our observations at 1.4 GHz. The sources found by Hyman et al.

---

[3] http://www.tauceti.caltech.edu/kunal/radio-transient-surveys/index.html
[4] https://github.com/ska-sa/katbeam

Figure 8. This figure shows the transient surface density versus the time-scale of the transient (on the left) and the faintest detectable transient (the sensitivity, on the right). The key shows the surveys included in this plot; these surveys are at 1.4 GHz and are for transient time-scales of less than 1 month. The red diamonds are the three surveys presented in this paper, on time-scales of 8 s, 128 s, and 1 h. The red curved lines show the sensitivity as a function of the surface density for each survey, taking into account the changing sensitivity across the images caused by the primary beam.

(2005) and Stewart et al. (2016) were detected on lower frequencies than our survey, which is why they are not plotted in Fig. 2.

On 1 h time-scales, we find an upper limit on the transient surface density of 3.2×10^{-2} deg^{-1} at a sensitivity of 3.9 mJy. From the sensitivity–surface density red curve presented in Fig. 8, we note that this survey constitutes the deepest transient survey on 1 h time-scales to date. The nearest comparable surveys (with durations of $\lesssim 1$ h; Frail et al. 2012; Alexander, Soderberg & Chomiuk 2015) have surface densities one to two orders of magnitude higher than the survey presented in this paper at a comparable sensitivity. On this time-scale and the 128 s time-scale, we might expect to detect flare stars in our local region of our Galaxy (see e.g. Andersson et al. 2022; Driessen et al. 2022). Detectable Galactic flare stars would be expected to be somewhat isotropically distributed across the sky due to their proximity to Earth and, hence, the high Galactic latitude of the field presented in this paper should not significantly impact upon the rates of detection.

6 DISCUSSION AND CONCLUSIONS

In this work, we present a blind radio transient survey on around 7 h of MeerKAT data. We have used a search radius of 1.4 deg in each image, and considered three time-scales to study: 8 s, 128 s, and 1 h. A total sky area of around 1.13×10^4, 7.04×10^2, 23.5 square degrees has been surveyed at a sensitivity of 56.4, 19.2, and 3.9 mJy for the 8 s, 128 s, and 1 h time-scales, respectively.

We have developed an imaging and filtering strategy to efficiently perform the transient survey, and we find that this method is faster and deeper than searching standard snapshots. The method is effective for finding faint short-duration transient phenomena in radio images, which makes it promising for future surveys. However, at the moment

it cannot be used to monitor variability. This is related to the continuum subtraction, as sources that are present in the deep image are subtracted from the visibilities. Since this can also result in some artefacts, we cannot reliably detect variable sources, for example, through detecting negative sources in the snapshot images, with the current imaging method. As interesting variable sources are currently being found through new MeerKAT commensal transient surveys (e.g. Driessen et al. 2022; Rowlinson et al. 2022), this would be interesting to explore in the future.

Further optimization can be implemented by reconsidering the `extraction_radius` as discussed in Section 4.1. As the telescope is the most sensitive in the primary beam, the `extraction_radius` can instead be set to the size of the HWHM of the telescope beam. We have also explored lowering the detection threshold for the survey. However, this resulted in a substantial increase of false positive candidates, as well as complicating the verification of transient candidates. Finally, the time-scales of 1 h, 128 s, and 8 s used for this short-duration transient survey were based on predicted and/or previously detected radio transients, such as slow-spin or eclipsing pulsars, solar bursts, and stellar flares for example (see e.g. Stewart et al. 2016; Caleb et al. 2022). However, as more short-duration transients are detected, we can use these results to characterize the optimal time-scales to probe in future surveys.

Once transient candidates are found, the data can be re-imaged to obtain properties such as the accurate flux density. It is important to note that the candidates should be sufficiently bright to achieve this, as the re-imaged data can probe higher values for the rms noise than the original images, as discussed in Section 4.3. Consequently, we were unable to recover the rejected transient candidate presented in this section. However, alternative methods can be used to determine if detected candidates are true astrophysical transients, for example, by

probing other radio observations of the same field, as well as through looking for counterparts in other observing bands. As the rejected transient candidate could potentially be a flare star, one could probe other MHONGOOSE observations of the same field, to confirm if transient emission is detected at the location of the candidate.

The one transient candidate detected in our transient survey was rejected because of our strict quality control settings. We tried a few methods to adjust our quality control settings, as discussed in Section 4.3, but this resulted in including evidently low-quality images as well. As the quality control method was developed for standard snap shot images, this might need adapting for similar data and methods in future work, for example, by evaluating the local image quality for transient candidates as well, instead of only evaluating the quality for the inner one-eighth of the image.

Moreover, we are able to place competitive limits on transient rates for the time-scales of 1 h (3.2×10^{-2} deg^{-1} at a sensitivity of 3.9 mJy) and 128 s (1.1×10^{-3} deg^{-1} at a sensitivity of 19.2 mJy), through analysing only 7 h of data. When comparing our findings to surveys at similar time-scales, we would expect to find one transient at the 128 s time-scale. If the rejected transient candidate presented in Section 4.3 is a true astrophysical transient, our results would be consistent with findings in other surveys. Finally, we also conducted one of the first commensal transient surveys of its kind on 8 s time-scales at 1.4 GHz.

By combining radio data from new facilities with excellent uv-coverage, and new rapid imaging and search strategies such as the methods presented in this work, we will be able to probe radio transients on time-scales from seconds to hours to high sensitivity. Facilities such as MeerKAT, ASKAP, and the highly anticipated SKA will allow us to make significant progress in studying short-duration image-plane radio transients.

DATA AVAILABILITY

The data and scripts underlying this article will be available in Zenodo at DOI: 10.5281/zenodo.7883761 upon publication. The MeerKAT data used are available in the MeerKAT data archive at https://archivesarao.ac.za/. The PanSTARRS fits images were obtained from https://panstarrs.stsci.edu.

REFERENCES

Alexander K. D., Soderberg A. M., Chomiuk L. B., 2015, ApJ, 806, 106
Andersson A. et al., 2022, MNRAS, 513, 3482
Andersson A. et al., 2023, MNRAS, 523, 2219
Aoki T. et al., 2014, ApJ, 781, 10
Becker R. H., White R. L., Helfand D. J., 1995, ApJ, 450, 559
Bell M. E. et al., 2011, MNRAS, 415, 2
Bell M. E. et al., 2014, MNRAS, 438, 352
Bhandari S. et al., 2018, MNRAS, 478, 1784
Bochenek C. D., McKenna D. L., Belov K. V., Kocz J., Kulkarni S. R., Lamb J., Ravi V., Woody D., 2020, PASP, 132, 034202
Bower G. C., Saul D., 2011, ApJ, 728, L14
Braun R., Bourke T., Green J. A., Keane E., Wagg J., 2015, Proc. Sci., Advancing Astrophysics with the Square Kilometre Array (AASKA14). SISSA, Trieste, PoS#174
CHIME/FRB Collaboration, 2018, ApJ, 863, 48
Caleb M. et al., 2022, Nat. Astron., 6, 828
Camilo F., 2018, Nat. Astron., 2, 594
Carbone D. et al., 2018, Astron. Comput., 23, 92
Carilli C. L., Ivison R. J., Frail D. A., 2003, ApJ, 590, 192
Chambers K. C. et al., 2016, preprint (arXiv:1612.05560)
Chastain S. I., van der Horst A. J., Rowlinson A., Rhodes L., Andersson A., Diretse R., Fender R. P., Woudt P. A., 2023, MNRAS, 526, 1888
Condon J. J., Ransom S. M., 2016, Essential Radio Astronomy. Princeton University Press, Princeton, NJ
Croft S., Bower G. C., Keating G., Law C., Whysong D., Williams P. K. G., Wright M., 2011, ApJ, 731, 34

de Blok W. J. G. et al., 2016, in Proceedings of MeerKAT Science: On the Pathway to the SKA. p. 7
de Blok W. J. G. et al., 2020, A&A, 643, A147
de Ruiter I., Leseigneur G., Rowlinson A., Wijers R. A. M. J., Drabent A., Intema H. T., Shimwell T. W., 2021, MNRAS, 508, 2412
Dobie D. et al., 2022, MNRAS, 510, 3794
Dobie D. et al., 2023, MNRAS, 519, 4684
Drake A. J. et al., 2009, ApJ, 696, 870
Driessen L. N. et al., 2020, MNRAS, 491, 560
Driessen L. N. et al., 2022, MNRAS, 512, 5037
Fender R. et al., 2016, in Proceedings of MeerKAT Science: On the Pathway to the SKA. p. 13
Finlator K. et al., 2000, AJ, 120, 2615
Frail D. A., Kulkarni S. R., Ofek E. O., Bower G. C., Nakar E., 2012, ApJ, 747, 70
Gaia Collaboration, 2016, A&A, 595, A1
Gourdji K., Rowlinson A., Wijers R. A. M. J., Broderick J. W., Shulevski A., Jonker P. G., 2022, MNRAS, 509, 5018
Hancock P. J., Drury J. A., Bell M. E., Murphy T., Gaensler B. M., 2016, MNRAS, 461, 3314
Hurley-Walker N. et al., 2022a, Publ. Astron. Soc. Aust., 39, e035
Hurley-Walker N. et al., 2022b, Nature, 601, 526
Hyman S. D., Lazio T. J. W., Kassim N. E., Ray P. S., Markwardt C. B., Yusef-Zadeh F., 2005, Nature, 434, 50
Johnston S. et al., 2008, Exp. Astron., 22, 151
Józsa G. I. G. et al., 2020, in Pizzo R., Deul E. R., Mol J. D., de Plaa J., Verkouter H., eds, ASP Conf. Ser. Vol. 527, Astronomical Data Analysis Software and Systems XXIX. Astron. Soc. Pac., San Francisco, p. 635
Kuiack M., Wijers R. A. M. J., Shulevski A., Rowlinson A., Huizinga F., Molenaar G., Prasad P., 2021, MNRAS, 505, 2966
Levinson A., Ofek E. O., Waxman E., Gal-Yam A., 2002, ApJ, 576, 923
Lorimer D. R., Bailes M., McLaughlin M. A., Narkevic D. J., Crawford F., 2007, Science, 318, 777
Mauch T. et al., 2020, ApJ, 888, 61
Mooley K. P., Frail D. A., Ofek E. O., Miller N. A., Kulkarni S. R., Horesh A., 2013, ApJ, 768, 165
Mooley K. P. et al., 2016, ApJ, 818, 105
Murphy T. et al., 2021, Publ. Astron. Soc. Aust., 38, e054
Offringa A. R., de Bruyn A. G., Biehl M., Zaroubi S., Bernardi G., Pandey V. N., 2010, MNRAS, 405, 155
Offringa A. R. et al., 2014, MNRAS, 444, 606
Petroff E., Hessels J. W. T., Lorimer D. R., 2022, A&AR, 30, 2
Pietka M., Fender R. P., Keane E. F., 2015, MNRAS, 446, 3687
Prasad P. et al., 2016, J. Astron. Instrum., 5, 1641008
Rowlinson A. et al., 2016, MNRAS, 458, 3506
Rowlinson A. et al., 2022, MNRAS, 517, 2894
Serra P. et al., 2019, A&A, 628, A122
Skrutskie M. F. et al., 2006, AJ, 131, 1163
Stappers B., 2016, in Proceedings of MeerKAT Science: On the Pathway to the SKA. p. 10
Stewart A. J. et al., 2016, MNRAS, 456, 2321
Swinbank J. D. et al., 2015, Astron. Comput., 11, 25
Thyagarajan N., Helfand D. J., White R. L., Becker R. H., 2011, ApJ, 742, 49
Virtanen P. et al., 2020, Nat. Methods, 17, 261
Wang Y., Tuntsov A., Murphy T., Lenc E., Walker M., Bannister K., Kaplan D. L., Mahony E. K., 2021, MNRAS, 502, 3294
Wang Z. et al., 2022, MNRAS, 516, 5972
Wang Y. et al., 2023, MNRAS, 523, 5661
Yu B., Zijlstra A., Jiang B., 2021, Universe, 7, 119

APPENDIX A: PREVIOUS TRANSIENT SURVEYS

Table A1 shows the transient surface density constraints at ≈ 1.4 GHz obtained using a range of transient surveys for transients with time-scales of less than 1 month. These data are used to plot Fig. 8 and were obtained from Mooley et al. (2016).[5]

---

[5]http://www.tauceti.caltech.edu/kunal/radio-transient-surveys/index.html

Table A1. Transient surface densities at ≈1.4 GHz obtained from Mooley et al. (2016).

Sensitivity (Jy)	Transient Surface Density (deg^{-2})	Time-scale (d)	Author
1.5×10^{-4}	<5.7	19	Carilli, Ivison & Frail (2003)
7×10^{-2}	$<3 \times 10^{-3}$	1	Bower & Saul (2011)
3	$<9 \times 10^{-4}$	1	Bower & Saul (2011)
0.35	$<6 \times 10^{-4}$	1	Croft et al. (2011)
8×10^{-3}	$<3.2 \times 10^{-2}$	4	Bell et al. (2011)
1×10^{-3}	6.5×10^{-3}	2×10^{-3}	Thyagarajan et al. (2011)
3.7×10^{-4}	<0.6	1.4×10^{-2}	Frail et al. (2012)
2.1×10^{-4}	<0.37	1	Mooley et al. (2013)
3	2×10^{-6}	1	Aoki et al. (2014)
5×10^{-4}	<17	2×10^{-2}	Alexander, Soderberg & Chomiuk (2015)
6×10^{-4}	$<8 \times 10^{-2}$	1	Mooley et al. (2016)
1.5×10^{-3}	<0.3	1	Bhandari et al. (2018)
1.5×10^{-3}	<0.3	12	Bhandari et al. (2018)
1×10^{-3}	$<3.7 \times 10^{-2}$	7	Rowlinson et al. (2022)
2×10^{-4}	3.2×10^{-4}	1.0×10^{-2}	Wang et al. (2023)
5.64×10^{-2}	$<6.7 \times 10^{-5}$	9.3×10^{-5}	This work (8 s)
1.92×10^{-2}	$<1.1 \times 10^{-3}$	1.5×10^{-3}	This work (128 s)
3.9×10^{-3}	$<3.2 \times 10^{-2}$	4.2×10^{-2}	This work (1 h)

This paper has been typeset from a TEX/LATEX file prepared by the author.